PERFORMANCE OF A PRECISION LOW FROST-POINT HUMIDITY GENERATOR

Gregory E. Scace, D. Christian Hovde, Joseph T. Hodges, Peter H. Huang, Joel A. Silver,* and James R. Whetstone*

Chemical Science and Technology Laboratory
National Institute of Standards and Technology
Gaithersburg, MD 20899

* Southwest Sciences Inc.
1570 Pacheco St. Suite E-11
Santa Fe, New Mexico 87505

Abstract: We discuss the performance of a new precision humidity generator designed to extend calibration capabilities at NIST from the current lower limit of 1.2 μmol to 3.4 nmol of water vapor per mole of gas mixture. The system comprises a copper saturator with ice-coated passageways, residing within an evacuated enclosure. The saturator temperature is actively regulated using thermoelectric devices and a mechanical refrigeration system for heat removal. Near-isothermal conditions within the saturator are achieved with high thermal conductivity materials, careful control of thermal boundary conditions and minimization of thermal loading from the laboratory environment. Temperature stability of the system is better than ±2.5 mK (two-sigma value). Maximum temperature differences in the saturator are less than 10 mK, and the uncertainty in temperature at the saturator outlet is estimated to be ≈10 mK. We discuss the results of an experimental intercomparison between the new generator and the NIST Mark-2 standard two-pressure generator over the frost-point range from −20 °C to −70 °C, and present direct measurements of the LFPG output water vapor concentration between 2.5 μmol/mol and 5 nmol/mol, using a 1.39 μm diode laser hygrometer based on wavelength modulation spectroscopy.

Keywords: Generator, standard, spectroscopy

1 INTRODUCTION

While there exist many applications of hygrometry spanning several decades of water vapor concentration, the emergence of new technologies places increasing emphasis on the measurement of water vapor mole fractions below 1 μmol /mol. For example, the strict monitoring and control of trace (10 nmol/mol and lower) levels is required in processes related to the fabrication of microelectronics and semiconductors. Regrettably, metrology-grade standards are not well established in the nmol/mol range, and existing hygrometers are inadequate as they often suffer from hysteresis, irreproducibility and relatively slow response times. Further, measurements of low humidity levels are complicated by poorly understood interactions between water vapor, carrier gases and transfer lines, as well as uncertainties in thermodynamic properties of ice/water vapor mixtures. To address these technical issues, it is useful to have devices for the precision generation of moisture

that enable the development of new hygrometer technologies and provide a link to primary standards of humidity measurement.

In this paper, we discuss the design and performance of a new thermodynamically based humidity generator, referred to as the low frost-point generator (LFPG). Its output spans six decades, covering the range 4 mmol/mol to 3.4 nmol/mol, in mole fraction of water vapor. A detailed description of the apparatus and measurements of the LFPG saturator temperature and pressure stability are presented. Finally, we discuss experiments characterizing the generator output over a subset of the operating range.

2 PRINCIPLE OF OPERATION

The LFPG saturates an inert gas stream with water vapor by flowing the gas over a plane surface of isothermal ice at known temperature and pressure. By ensuring that the inlet gas stream has reached thermodynamic equilibrium with the generator saturator, the mole fraction of water vapor in the gas phase, x_w, can be calculated from first principles, and is proportional to the vapor pressure of the ice, $e_w(T)$ and the so-called enhancement factor, $f(T,P)$. This factor is close to unity and accounts for departures from ideal solution behavior as well as non-ideal gas effects [1,2]. Assuming that the saturator ice and sample stream are in local thermodynamic equilibrium, then, at a total pressure, P_s , and system absolute temperature , T_s ,the mole fraction of water vapor is

$$x_w = \frac{e_w(T_s)}{P_s} \cdot f(T_s,P_s) \qquad (1)$$

in which the subscript, *s*, indicates conditions in the saturator. Equation 1 represents the central theoretical basis for the use of the low frost-point generator as a humidity standard. The predicted values of LFPG-produced water vapor mole fractions cited in this paper are based on the ice vapor pressure correlation of Wexler [1] and the enhancement factor equation for water vapor/air mixtures [2], both of which are referenced to IPTS-68. To use these equations, the measured temperatures (which are referenced to ITS-90) are first converted to IPTS-68 [3].

Measurements of the gas frost-point temperature made downstream of the saturator (as for example with a chilled mirror hygrometer) must be related to the saturator conditions. Assuming that the water vapor mole fraction is conserved, and assuming that the chilled mirror and sample stream are in local thermodynamic equilibrium, then,

$$x_w = \frac{e_w(T_s)}{P_s} \cdot f(T_s,P_s) = \frac{e_w(T_h)}{P_h} \cdot f(T_h,P_h) \quad , \qquad (2)$$

in which the subscript *h*, indicates conditions in the hygrometer.

3 DESIGN DETAILS OF THE LFPG

3.1 General component description

The LFPG consists of a saturator residing within an evacuated enclosure, plumbing and flow control for the carrier gas, and associated temperature and pressure measuring instrumentation. A multi-mode, closed loop temperature control scheme comprising Peltier heat-pump thermoelectric devices (TEDs) and a mechanical refrigeration system maintains saturator temperature stability, and allows rapid adaptation to relatively large changes in heat loading. The upper limit in generated water vapor is set by the maximum practical operating temperature of $-5\,^{\circ}C$, corresponding to 4 mmol/mol. The minimum mole fraction achievable by the LFPG, 3.4 nmol/mol, is set by the minimum attainable saturator temperature of $-101.6\,^{\circ}C$ and the maximum allowable saturator pressure of $\approx 3 \cdot 10^5$ Pa. A simplified description of the LFPG design follows. A more complete description can be found in Ref. 4.

Seven stacked, oxygen-free high-conductivity copper disks, each 195 mm in diameter and 18.5 mm thick, comprise the saturator. A diagram of the saturator with numbered disks is given in Fig. 1. Machined recesses in the outer faces of the top and bottom plates mate with two arrays (one on plate 1 and the other on plate 7) of four TEDs per array. Plates 1 and 7 act as spacers between the TEDs and the saturator passageway, and attenuate temperature gradients that might occur at the TED-saturator interface. Spiral grooves machined into the bottom faces of plates 2 through 5 form a passageway of square cross section, 4.88 m in length, containing the ice layer. In plate 6, a thermometer well, drilled radially with its centerline 7 mm below the bottom of plate 5 houses a 25 Ω encapsulated standards-grade platinum resistance thermometer (SPRT). A pressure tap runs radially to the center of plate 6. All seven plates were electroless nickel plated for corrosion resistance and brazed together in a vacuum furnace using the nickel plating as the brazing filler material.

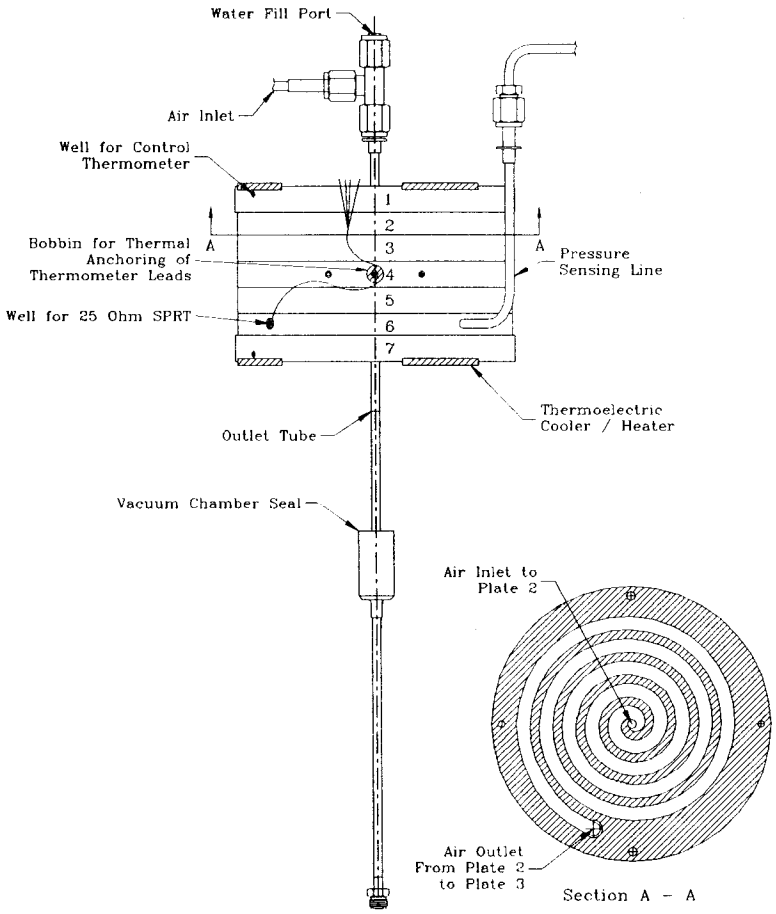

Figure 1. LFPG Saturator

The saturator temperature is controlled by axial heat pumping. An ohmmeter measures the resistance of

two 100 Ω SPRTs, one each located at the top and bottom faces of the saturator. Using these temperature data as feedback in a servo-loop, two proportional-integral-derivative (PID) control algorithms control current supplied to the upper and lower TED arrays, simultaneously minimizing the differences between the top and bottom saturator face temperatures and between the average saturator and setpoint temperatures. Heat pumped from the saturator is removed from the vacuum environment by expanding liquified ethylene to the vapor phase within a pair of cylindrical refrigeration plates in contact with the TEDs. An independent PID controller within the refrigeration system maintains the desired refrigeration plate temperature.

A vacuum chamber surrounding the saturator and located within an insulated box provides a high degree of thermal isolation from the surroundings. The chamber pressure, $\approx 8 \cdot 10^{-4}$ Pa, is sufficiently low to effectively eliminate molecular heat conduction and gas phase heat convection within the chamber. Three radiation shields encircling the saturator (two of copper and one of aluminized polymeric film) minimize radiation heat transfer from the vacuum chamber walls to the saturator. Near −100 °C, the transient warmup rate of the saturator, with the temperature control systems inactive, was measured to be ≈0.5 mK/s. This translates into a thermal loading of about 10 W.

3.2 Instrumentation

As shown in Eq.1, the prediction of LFPG-generated water vapor mole fraction requires measurement of the saturator temperature and pressure. Additionally, to calculate the frost-point temperature sensed by a chilled-mirror hygrometer, the pressure at the mirror must also be known (see Eq. 2).

A quartz Bourdon tube pressure gage (range 0 − 300 kPa) measures the absolute gas pressure at the saturator outlet. The gas pressure at the hygrometer mirror is approximated using the barometric pressure measured by a piezo-resistive gage. Both pressure gages are calibrated with a dead weight testing system having a relative expanded uncertainty of $40 \cdot 10^{-6}$ Pa/Pa (coverage factor, k, equal to two). The expanded uncertainties for both pressure measurements are 13 Pa ($k = 2$).

A 25 Ω SPRT oriented radially in plate 6 measures the saturator temperature. The thermometer resistance is calculated by measuring the ratio of voltage drops across the thermometer and a 100 Ω standard resistor at a constant current of ≈1 mA. The expanded uncertainty ($k = 2$) of the temperature measurement is a function of temperature and arises from three sources; current instability, voltmeter non-linearity and the uncertainty of the thermometer calibration. For temperatures equal to −100 °C, −50 °C and 0 °C, the expanded uncertainties are, 1.7 mK, 2.3 mK and 2.8 mK, respectively. The overall temperature uncertainty must incorporate the effects of temperature gradients within the saturator.

3.3 Preparation of LFPG for use

To fill the saturator, 140 cm^3 of distilled water is slowly introduced into the top of the saturator with a syringe. Dams in each saturator stage allow the water to pool to a depth of 2.5 mm.

For the generator to produce the expected results, the saturator must be the only source of water in the sample gas. Potential sources, such as plumbing downstream of the saturator, must be minimized, especially for measurements at the lowest concentrations. Any liquid phase water downstream of the saturator is removed by flushing the pressure sensing line and saturator outlet tubing with dry nitrogen (water mole fraction < 10 nmol/mol) from a liquid nitrogen dewar. This flow path bypasses the saturator itself and flushes all tubing downstream of the saturator. After several hours of flushing at room temperature, the saturator temperature is reduced to −5 °C, and the water is frozen. Typically, dry nitrogen is used to continuously flush all downstream plumbing for at least five days after freezing the water in the saturator. During both preparation and normal operation, the saturator outlet tube is heated to 100 °C.

4 GENERATOR PERFORMANCE

This section discusses the measurement and assessment of uncertainties in generator parameters required to predict moisture content of the sample gas. We also present the realization of predicted humidities through measurement of the generator's output and comparison with other standards, where possible. While uncertainies in measured temperatures and pressures have been quantified, an overall LFPG uncertainty has yet to be assigned.

4.1 Saturator temperature stability and gradients

The saturator temperature stability dominates the overall LFPG performance since the ice vapor pressure varies exponentially with temperature [1]. The stability is limited by the speed, resolution and stability of the ohmmeter used to measure the control thermometer resistance, and by the ability of the TED control system to compensate for fluctuations in the heat load from various sources such as pulsing of refrigerant through the refrigeration plates. Figure 2 shows typical temperature stability attained by the LFPG at −101.6 °C and −45 °C as measured by the 25 Ω SPRT. At −101.6 °C, the two-sigma value for fluctuations about the setpoint is 2.2 mK. At −45 °C, the steady state temperature fluctuation about the mean is less than 1.25 mK (two-sigma value). At a fixed saturator pressure, the two-sigma values for the deviation in generated water vapor concentration are ±0.015% at −45 °C and ±0.045% at −101.6 °C.

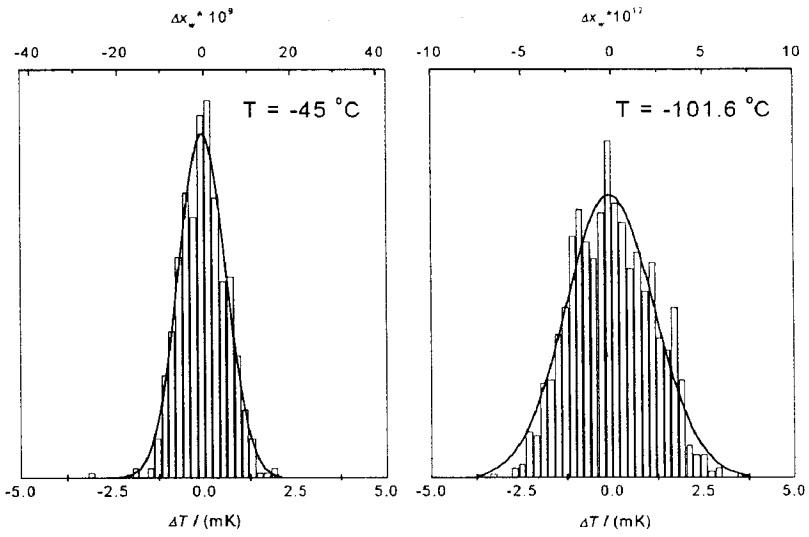

Figure 2. Distributions of LFPG saturator temperature about the mean value at setpoints of −45 °C and −101.6 °C, corresponding to water vapor mole fractions in air of 72 μmol/mol and 10 nmol/mol, respectively. The top axis represents the corresponding change in equilibrium water vapor mole fraction from the mean value. Solid lines represent Gaussian fits to the distributions. These results are based on measurements spanning several hours.

While boundary temperature conditions are imposed by the TED arrays and the associated control system, temperature gradients exist within the saturator due to radiative heat exchange between the vacuum chamber walls and the saturator, heat conduction along plumbing connected to the saturator, and sensible heat exchange inside the saturator associated with cooling the carrier gas. Temperature differences were measured with the 25 Ω SPRT and another 100 Ω SPRT, axially located midway between the top and bottom faces, and buried to a depth of 2 cm, close to the pressure tap. This location probably experienced the largest measurable temperature difference due to its proximity to the pressure tap. At a flow rate of 2 L/min and throughout the operating temperature range of the generator, the upstream temperature was found to be less than 10 mK warmer than that recorded by the 25 Ω SPRT. Variation in this measured temperature difference due to different generator flow rates was also assessed at saturator temperatures of −30 °C and −100 °C. Deviation from the flow rate of 2 L/min affected the measured temperature difference by +0.75 mK/(L/min) and +1.8 mK/(L/min), respectively.

For the test air to achieve temperature equilibrium with the ice and become saturated with water vapor, it must spend sufficient time in contact with the ice. To assess whether the exiting air and saturator are in thermal equilibrium, we estimated the air and ice temperature as a function of distance along the saturator passageway using a one-dimensional steady state heat transfer model. These calculations suggest that the system behaves as a highly efficient heat exchanger by virtue of its relatively low thermal resistance and the long residence time of the air. At a setpoint temperature of −100 °C and a flow rate of 2 L/min, the characteristic decay length associated with exponential reduction of the gas stream temperature is about 19 cm. Given that the ice-coated channel within the saturator extends more than 25 decay lengths, temperature differences between the exiting air and saturator should be negligible. Also, to the extent that small temperature gradients exist in the flow direction (as discussed above), this relatively short decay length means that the temperature of the air exiting the saturator will be in local equilibrium with conditions near the saturator outlet.

4.2 Saturator pressure stability

As shown in Eq. 1, variations in saturator pressure influence the value of x_w. The variation of saturator pressure within the LFPG saturator equals the change in barometric pressure since at fixed flow rates, the pressure drop within the outlet tubing remains constant. The mole fraction of water vapor contained in the gas exiting the LFPG changes with saturator pressure by only 0.001 %/Pa of the nominal value. Consequently, the effect of atmospheric pressure fluctuations on LFPG-generated frost-point temperatures, measured by a chilled-mirror hygrometer at atmospheric pressure, is negligible. As an example, given a pressure drop of 500 Pa from the saturator to the hygrometer sensor, the frost-point temperature changes by less than 0.5 mK per 1000 Pa change in barometric pressure.

5 MEASUREMENTS OF LFPG OUTPUT

We have begun a long-term intercomparison between the LFPG and the Mark-II humidity generator (2-P). The latter is a two pressure generator whose output has been measured using the NBS Standard Gravimetric Hygrometer down to a frost-point temperature of −20 °C, and it has been used for research and calibration at NBS and NIST for nearly 25 years [5]. Since the LFPG will be

commissioned to provide calibration services over a range of operation that overlaps that of the 2-P, we are interested in quantifying the level of agreement between the two. The maximum expanded uncertainty ($k = 2$) of the 2-P generated frost-point is 50 mK above −20°C frost-point temperature, 70 mK between −20 °C and −40 °C, and 140 mK for frost-point temperatures below −40 °C. Below, we report some initial studies in which water vapor/air mixtures from 1023 µmol/mol to 544 nmol/mol (frost-points from −20 °C to −80 °C), produced by the LFPG, were monitored by a chilled-mirror hygrometer (CMH) that was previously calibrated by the 2-P.

We also report some preliminary direct measurements of the LFPG water vapor concentration based on wavelength modulation spectroscopy. As with the CMH experiments, air was used as the carrier gas. These data cover the range 2.5 µmol/mol down to 5 nmol/mol mole fraction of water vapor, near the LFPG lower limit of 3.4 nmol/mol.

5.1 Generator intercomparison

The CMH has a three-year calibration history against the 2-P. The measured resistances, R_i, of the CMH platinum resistance thermometer (PRT) obtained over this period were correlated with frost-point temperature, t_i, calculated from the measured temperature and pressure in the 2-P as well as with the CMH pressure (see Eq. 2), according to a fourth order equation of the form

$$R(R_o, a, b, c; t) = R_0[1 + at + bt^2 + ct^3(t - 100°C)] \quad . \tag{3}$$

The coefficients R_0 , a, b, c, were obtained through a least squares fit of the set of resistance/temperature data, (R_i, t_i). The coefficients (R_0, a, b, c) are (100.06036 Ω, $3.9056502 \cdot 10^{-3}$/°C, $-7.4661903 \cdot 10^{-7}$/°C^2, $1.9745613 \cdot 10^{-11}$/°C^4), respectively [4]. The residuals of each calibration data pair,

$$\delta t_i(R_i, t_i) = t(R_0, a, b, c; R_i) - t_i \ , \tag{4}$$

were calculated in which $t(R_0, a, b, c; R) = R^{-1}(R_0, a, b, c; R)$. The dashed line in Fig. 3, which represents a smooth curve through these residuals, systematically departs from zero. These results indicate that while Eq. 3 is often used to represent the behavior of industrial grade platinum resistance thermometers, it does not completely describe the response of the CMH to water/air mixtures produced by the 2-P or LFPG.

Over the subsequent nine months, the CMH was connected to the output of the LFPG and its mean resistances, R_j, were measured at various frost-point temperatures, t_j, from −20 °C to −80 °C. The measured resistances were converted to frost-point temperature by the inverse of Eq. 3. Residuals between the predicted frost-point based on measured LFPG temperature, pressure and hygrometer pressure, were calculated similarly to the 2-P data, using the coefficients given above. The solid line in Fig. 3 represents a smooth curve through the LFPG residuals, also systematically departing from zero. For both curves shown in Fig. 3, the error bars are given by ±2σ, in which σ is the local

standard deviation of the predicted value given by the respective residual fit. Comparison of the two sets of residuals gives the level of agreement between the two humidity generators. These data reveal a systematic difference between the two generators that increases with decreasing temperature from a minimum value of 30 mK at −35 °C to 100 mK at −70 °C. We note, however, that the maximum difference between the two is still within the estimated expanded uncertainty of the 2-P [6].

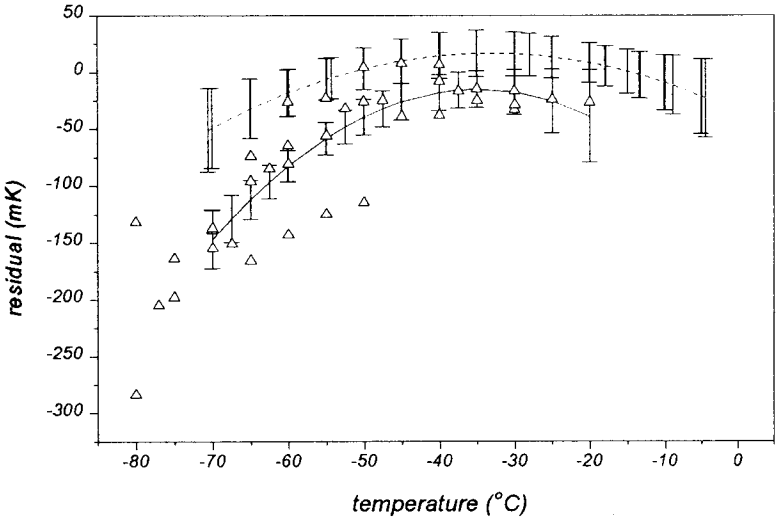

Figure 3. Chilled-mirror hygrometer intercomparison of LFPG and 2-P. The dashed line represents a smooth curve through the 2-P residuals, and the solid line represents a similar fit to the LFPG residuals. The error bars represent ±2σ of the predicted values estimated from the curve fits, and the open symbols are the measured LFPG residuals.

The LFPG data in Fig. 3 exhibit a significant amount of scatter which, given the high temperature and pressure stability of the LFPG discussed above, cannot be explained in terms of LFPG performance. Instead, this is attributed to irreproducibilities in the CMH determination of the frost-point temperature. We speculate that this behavior may arise from uncontrolled variation in the CMH ice morphology (*e.g.*, thickness, distribution, and crystalline structure) encountered from one experiment to another. Changes in any of these properties of the CMH ice layer could affect its equilibrium response. It is worth noting that the data comprise various sequences of LFPG setpoint temperatures obtained with a given ice layer on the CMH. Some data were obtained by forming ice on the CMH at relatively high temperatures (near 0 °C) and thereafter stepping downward in LFPG temperature. Other sets were obtained by forming the ice at the lowest accessible temperature and thereafter increasing the LFPG temperature. Each sequence of data was found to exhibit a smooth temperature dependence, yet no consistent correlation between the direction of temperature change and CMH response could be established upon multiple experimental realizations.

5.2 Wavelength modulation spectroscopy (WMS)

This technique, which is similar to frequency modulation spectroscopy (FMS), is based upon the absorption of electromagnetic radiation by a gas. Both WMS and FMS have been applied to many chemical species including water vapor, and absorbance noise levels as low as 10^{-7} have been achieved [7-11]. For sufficiently strong absorption transitions, such high sensitivity enables the detection of water vapor from μmol/mol to below nmol/mol levels.

When the absorbance, α_ν, of a laser beam propagating through a sample of length ℓ, is small (optically thin conditions), it is given by

$$\alpha_\nu = n\, g(P,T,\eta;\nu-\nu_0) S(T) \ell \quad , \tag{5}$$

where n is the number density of the absorbing species, $g(P,T,\eta;\nu-\nu_0)$ is the known transition lineshape function, $\nu-\nu_0$ is the frequency detuning of the probe laser about the center of the transition located at frequency ν_0, T is the measured sample temperature, and η and S are the broadening coefficient and line strength, respectively, of the rovibronic transition to which the probe laser is tuned. As a consequence of the wavelength modulation and phase-sensitive detection at twice the modulation frequency used in WMS, the output signal is approximately proportional to $d^2g/d\nu^2$; however, the exact response is modeled using a direct Fourier calculation of a modulated Voigt line shape. By scanning the laser frequency over a specific transition, n can be determined by a least squares fit of the WMS second harmonic signal to a model that includes the exact line shape and a quadratic background. For the temperature and pressure conditions in the WMS cell, the gas mixture behaves as an ideal gas, and it follows that WMS-measured water vapor mole fraction, $x_{w,WMS}$ is given by nRT/P where R is the universal gas constant. More details about the principle of operation of the WMS method can be found in Refs. 8 and 12.

In this experiment, absorption measurements were made with a distributed feedback (DFB) laser emitting near 1.39 μm. The DFB laser beam was coupled into a multi-pass cell having a total pathlength ℓ = 46.6 m, with an effective sample volume of 4000 cm^3. The beam exiting the cell was monitored by an InGaAs photodetector, and the resulting signal was measured with a lock-in amplifier at the second harmonic of the modulation frequency. A fraction of the sample gas from the LFPG was metered into the WMS cell using a critical flow orifice. Conditions within the WMS cell were maintained at a total gas pressure of $1.33 \cdot 10^4$ Pa (100 torr) and at a temperature near 22 °C.

The correspondence between $x_{w,WMS}$, and the predicted LFPG output water vapor mole fraction, x_w, is shown in Fig. 4. The solid line represents a linear fit to these data. The WMS measurements exhibit over two decades of

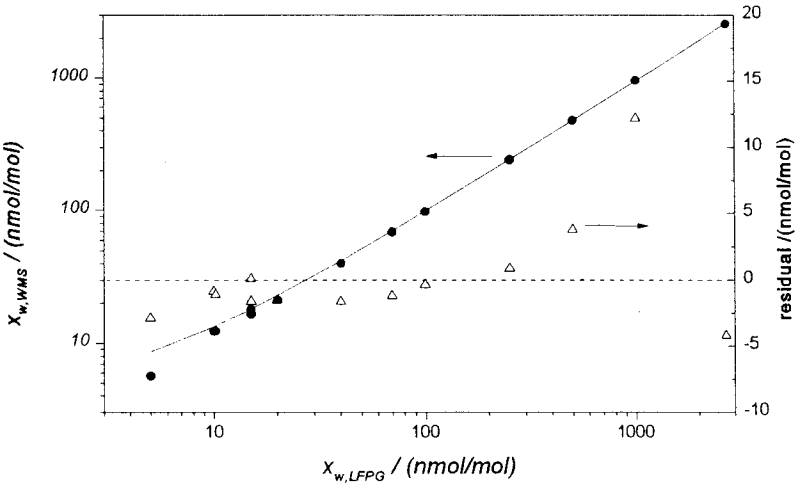

Figure 4. Solid circles represent absolute determination of LFPG generated water vapor mole fraction as measured by WMS (left axis), and the solid line is a linear fit to the WMS data. Triangles correspond to the difference between $x_{w,WMS}$ and the predicted value of water vapor mole fraction, where the predicted values are based on the linear fit to the WMS data (right axis).

linearity, but show a small, nonzero intercept. This intercept is associated with the background level of water vapor contributed by outgassing within the transfer lines downstream of the LFPG saturator and WMS sample cell. Using the values $S = 1.8 \cdot 10^{-20}$ cm^2 cm^{-1}/molecule and $\eta = 1.0017 \cdot 10^{-6}$ cm^{-1}/Pa published in the HITRAN database [13], and the ice vapor pressure correlation reported by Wexler [1], the linear regression to the data gives $x_{w,WMS} = 3.8$ nmol/mol + 0.95 x_w. This result corresponds to only a 5 % correction on the HITRAN value of S. Also shown in Fig. 4 are the residuals to the linear fit of the data (indicated by open triangles).

We note that the intercept of the linear fit may not be the best estimate of the background level of water vapor. Below $x_w \lesssim 100$ nmol/mol, the mean magnitude of the residuals is 1.2 nmol/mol. Therefore, our best estimate of the background water vapor mole fraction is 2.6 nmol/mol, instead of the 3.8 nmol/mol value corresponding to the intercept of the linear fit. For the measurements reported here, the data were obtained over several days during which time the system continued to dry out and background levels continued to decrease. For the smallest x_w reported here, this uncertainty in the background is significant. Better estimates of the background x_w would be required for more accurate measurements of the water vapor mole fraction in this range. This would require waiting sufficiently for the background to decay to a negligible level or reach a constant value.

Most of the background signal originated within the WMS sample cell. At constant LFPG generated water vapor mole fraction, variation of the sample gas flow rate through the WMS cell (accomplished by changing the LFPG saturator pressure upstream of the orifice plate) resulted in changes in $x_{w,WMS}$. However, at fixed WMS flow rate, $x_{w,WMS}$ was found to be nearly independent of the flow rate through the LFPG saturator. Thus, the value of 2.6 nmol/mol background mole fraction is an estimate of the nominal water vapor background contributed by the WMS sample cell.

It is interesting to note that the combined stability of the LFPG and the WMS was such that the WMS response was stable to within 0.25 % over time intervals as long as several hours. Furthermore, changes in the LFPG output as small as $\Delta x_w \lesssim 0.2$ nmol/mol were detectable.

6 CONCLUSION

The LFPG will extend NIST's humidity calibration capability from a lower limit of 1.2 μmol to 3.4 nmol of water vapor per mole of gas, and serve as a research tool facilitating the development of new measurement standards and low humidity measurement techniques. The temperature stability of the LFPG is within ±2.5 mK of the setpoint temperature, resulting in gas streams with vapor mole fractions which are expected to be constant to within 0.045%. Based on an intercomparison between the LFPG and the well-established NIST 2-P, the two systems agree to within the expanded uncertainty of the latter. In the humidity range 2.5 μmol/mol down to 5 nmol/mol, WMS measurements of the LFPG output showed good linearity and were consistent with the predicted generator performance.

7 ACKNOWLEDGMENTS

We would like to thank R. Cutkosky for developing the PID-control algorithm used to drive the TED arrays. Also, we take this opportunity to thank R. Hyland, R.I. Scace, C. W. Meyer, and G. J. Rosasco for carefully reading the manuscript and offering many helpful suggestions.

REFERENCES

1. A. Wexler, "Vapor pressure formulation for ice," Jour. Res. NBS, **81A**, 5-19 (1977).

2. R.W. Hyland and A. Wexler, "The enhancement of water vapor in carbon dioxide-free air at 30, 40, and 50 °C," Jour. Res. NBS, **77A**, 115-131 (1973).

3. H. Preston-Thomas and T.J. Quinn, Techniques for Approximating the International Temperature Scale of 1990, (Bureau International des Poids et Mésures, Pavillon de Breteuil, F-92310 Sèvres, First ed., 1990), Appendix A.

4. G.E. Scace, P.H. Huang, J.T. Hodges, D.A. Olson, and J.R. Whetstone, "The new NIST low frost-point humidity generator," *Proceedings of NCSL 1997 Workshop and Symposium*, Atlanta, USA, 657-674 (1997).

5. S. Hasegawa and J.W. Little, "The NBS two-pressure humidity generator, Mark-2," Jour. Res. NBS, **81A**, 81-88 (1977).

6. P.H. Huang, "Determining uncertainties in standard dew/frost-point generators for humidity measurements," *6th Intl. Symposium on Temperature and Thermal Measurement in Industry and Science*, Torino, Italy, 577-582, (1997).

7. J. Reid and D. Labrie, "Second-harmonic detection and tunable diode lasers - comparison of experiment and theory," Appl. Phys. B, **26**, 203-210 (1981).

8. J.A. Silver, "Frequency modulation spectroscopy for trace species detection: theory and comparison among experimental methods," Appl. Opt., **31**, 707-717 (1992).

9. J.A. Silver and D.C. Hovde, "Near-infrared diode laser airborne hygrometer," Rev. Sci. Instrum., **65**, 1691-1694 (1994).

10. J.J.F. McAndrew and R.S. Inman, "Using diode laser spectroscopy to evaluate techniques for acceleration of etch chamber evacuation," J. Vac. Sci. Technol. A, **14**, 1266-1272 (1996).

11. D.C. Hovde and C.A. Parsons, "Wavelength modulation detection of water vapor with a vertical cavity surface-emitting laser," Appl. Opt., **36**, 1135-1138 (1997).

12. J.M. Supplee, E.A. Whittaker, and W. Lenth, "Theoretical description of frequency modulation and wavelength modulation spectroscopy," Appl. Opt., **33**, 6294-6302 (1994).

13. L.S. Rothman, R.R. Gamache, R.H. Tipping, C.P. Rinsland, M.A.H. Smith, D.C.Benner, V. Malathy Devi, J.M. Flaud, C. Camy-Peyret, A. Perrin, A. Goldman, S.T. Massie, L.R. Brown, and R.A. Toth, "The HITRAN molecular database: editions of 1991 and 1992," J. Quant. Spectrosc. Radiat. Transfer, **48**, 469-507 (1992).

Contact point: Gregory E. Scace, National Institute of Standards and Technology, Chemical Science and Technology Laboratory, Process Measurements Division, Bldg. 221 Rm B128, Gaithersburg, MD, USA, 20899.

Telephone (301) 975-2626
Email gregory.scace@nist.gov